Title
Single-molecule superresolution imaging allows quantitative analysis of RAF multimer formation and signaling

Journal
Proceedings of the National Academy of Sciences of the United States of America, 110(46)

ISSN
0027-8424

Authors
Nan, Xiaolin
Collisson, Eric A
Lewis, Sophia
et al.

Publication Date
2013-11-12

DOI
10.1073/pnas.1318188110

Peer reviewed

Single-molecule superresolution imaging allows quantitative analysis of RAF multimer formation and signaling

Xiaolin Nan[a,b,1,2], Eric A. Collisson[b,c], Sophia Lewis[b], Jing Huang[b], Tanja M. Tamgüney[c], Jan T. Liphardt[a], Frank McCormick[c], Joe W. Gray[b,c,1,2], and Steven Chu[d,2]

[a]California Institute for Quantitative Biosciences, University of California, Berkeley, CA 94720; [b]Life Sciences Division, Lawrence Berkeley National Laboratory, Berkeley, CA 94720; [c]Helen Diller Family Comprehensive Cancer Center, University of California, San Francisco, CA 94158; and [d]Departments of Physics, and Molecular and Cellular Physiology, Stanford University, Stanford, CA 94305

Contributed by Steven Chu, October 2, 2013 (sent for review October 5, 2012)

The RAF serine/threonine kinases regulate cell growth through the MAPK pathway, and are targeted by small-molecule RAF inhibitors (RAFis) in human cancer. It is now apparent that protein multimers play an important role in RAF activation and tumor response to RAFis. However, the exact stoichiometry and cellular location of these multimers remain unclear because of the lack of technologies to visualize them. In the present work, we demonstrate that photoactivated localization microscopy (PALM), in combination with quantitative spatial analysis, provides sufficient resolution to directly visualize protein multimers in cells. Quantitative PALM imaging showed that CRAF exists predominantly as cytoplasmic monomers under resting conditions but forms dimers as well as trimers and tetramers at the cell membrane in the presence of active RAS. In contrast, N-terminal truncated CRAF (CatC) lacking autoinhibitory domains forms constitutive dimers and occasional tetramers in the cytoplasm, whereas a CatC mutant with a disrupted CRAF–CRAF dimer interface does not. Finally, artificially forcing CRAF to the membrane by fusion to a RAS CAAX motif induces multimer formation but activates RAF/MAPK only if the dimer interface is intact. Together, these quantitative results directly confirm the existence of RAF dimers and potentially higher-order multimers and their involvement in cell signaling, and showed that RAF multimer formation can result from multiple mechanisms and is a critical but not sufficient step for RAF activation.

cancer signaling | single molecule imaging | superresolution optical microscopy

The RAF serine/threonine protein kinase is a component of the three-tiered MAPK signaling pathway that regulates cell growth and many other essential biological processes (1, 2). In normal cells, extracellular mitogenic stimuli are transmitted to the nucleus via the receptor–RAS–RAF–MAPK cascade (2). Abnormal activation of this pathway is a central event in many human cancers and results from activating mutations in *BRAF* itself or in upstream factors (such as the *RAS* genes) (3, 4). As the RAS proteins so far are intractable pharmacologic targets (5), attention has shifted to development of small-molecule RAF inhibitors (RAFis) as antitumor therapeutic agents (6). To date, RAFi clinical efficacy has been demonstrated only for $BRAF^{V600E}$ melanoma (6–8). In tumors with WT *BRAF* or mutant *RAS*, most RAFis paradoxically promote growth, at times malignant in nature (6). Moreover, *BRAF* mutant melanomas that are initially sensitive to RAFi rapidly become resistant by using a variety of compensatory mechanisms including RAF isoform switching and activation of other pathways including RTKs, RAS, or PI3K (9). In addition, some RAFis (e.g., vemurafenib) accelerate the occurrence of secondary squamous cell carcinomas (10).

Several lines of investigation suggest that multimer formation plays an important role in RAF activation and tumor responses to RAFi (11–16). RAF dimerization-mediated signaling was first suggested by the observation that artificial dimerization activates RAF (17, 18). Next, immunoprecipitation (IP) suggested that formation of homo- and heterotypic RAF "dimers" is associated with active RAS (15, 16, 19). X-ray crystallography of the BRAF catalytic domain (CatB) identified critical residues postulated to enable CatB–CatB dimer formation (11). Mutations of these residues (e.g., R509H in BRAF and, equivalently, R401H in CRAF) profoundly diminished dimerization and kinase activity of RAF (11–13). Recently, dimerization also was implicated in RAFi-mediated activation of RAF in $BRAF^{WT}$ tumors (12, 13), in acquired resistance of $BRAF^{V600E}$ tumors to RAFi (14), and in the development of RAFi-induced secondary squamous carcinomas (10).

Although these studies implicate RAF multimer formation in the regulation of signaling in some circumstances, they do not provide direct characterization of the nature of these multimers, nor the information about their intracellular locations. This is in a large part because of the lack of techniques with sufficient spatial and stoichiometric (protein counting) resolution to visualize RAF multimers inside an intact cell. For example, X-ray crystallography studies used purified and truncated RAF proteins (11, 20). IP measures protein–protein interactions but does not provide stoichiometric or cellular localization information of the protein complexes (12, 13).

Significance

This paper describes a quantitative imaging approach based on photoactivated localization microscopy for precise protein localization and stoichiometric analysis inside an intact cell. With this approach, we directly resolved individual protein monomers, dimers, and multimers in fixed mammalian cells. We used this technique to study the dimerization and multimerization of the protein kinase RAF, a putative mechanism for mutant *Rat sarcoma* (RAS)-mediated RAF activation as well as for the paradoxical activation of RAF/MAPK in RAF WT cells and tumors upon treatment with RAF kinase inhibitors. We presented direct evidence that RAF indeed forms dimers and occasionally higher-order multimers under various activating conditions. These observations provide critical insight into the biological regulation of RAF signaling and oncogenesis.

Author contributions: X.N., E.A.C., F.M., J.W.G., and S.C. designed research; X.N., E.A.C., S.L., J.H., and T.M.T. performed research; X.N. analyzed data; X.N., E.A.C., F.M., J.W.G., and S.C. wrote the paper; and J.T.L. facilitated management of research.

The authors declare no conflict of interest.

Freely available online through the PNAS open access option.

[1]Present address: Department of Biomedical Engineering, Knight Cancer Institute, and OHSU (Oregon Health and Science University) Center for Spatial Systems Biomedicine, Oregon Health and Science University, Portland, OR 97239.

[2]To whom correspondence may be addressed. E-mail: nan@ohsu.edu, grayjo@ohsu.edu, or schu@stanford.edu.

This article contains supporting information online at www.pnas.org/lookup/suppl/doi:10.1073/pnas.1318188110/-/DCSupplemental.

The foregoing studies underscore the need for better tools to study the RAF complexes involved in cell signaling. In the present work, we show that recently introduced single-molecule superresolution imaging techniques such as photoactivated localization microscopy (PALM) (21, 22) can be used for direct, quantitative analysis of RAF multimer formation inside an intact mammalian cell. We first demonstrate that PALM provides sufficient spatial and stoichiometric resolution to distinguish artificial protein dimers and higher-order multimers from monomers when using a suitable fluorescent probe and combined with quantitative spatial analysis. We then apply the quantitative PALM imaging approach to study CRAF multimerization under resting and various activating conditions, including the presence of active mutant RAS, N-terminal truncation, and artificial membrane localization. Our results clearly indicate the formation and significance of RAF dimers in cell signaling. The biological and therapeutic implications of these results are discussed.

Results

PALM Imaging for Assessment of Protein Multimerization. In PALM imaging, cells are genetically engineered to express one or more photoactivatable fluorescence protein (PA-FP). If the PA-FP is attached to a protein of interest, locations of the PA-FP report the locations of the protein of interest. PALM image acquisition is an iterative process. Each iteration begins with photoactivation of PA-FP molecules typically by UV illumination followed by excitation at a longer wavelength selected to stimulate fluorescence from the activated fluorophore. The intensity of the photoactivation is controlled so that only a few PA-FPs are activated at once. Each activated PA-FP molecule forms a diffraction-limited and isolated image on the detector, of which the center can be localized to within 10 to 20 nm in the imaging plane. Fluorescence from activated PA-FPs is collected until extinguished by permanent photobleaching or by entry of the molecules into transient dark states (or "blinking"). Successive rounds of PA-FP activation, illumination, and imaging continue until PA-FPs in the sample are depleted. The resulting fluorophore locations are combined computationally into one image showing the locations of the individual PA-FP molecules localized with 10 to 20 nm precision (21–23) to provide the final, high-resolution PALM image of the sample.

The biochemical and photophysical properties of the PA-FP may have a profound impact on how authentically the PALM image reflects the properties of the sample. For quantitative, stoichiometric measurements with PALM, the PA-FP should have a high photon yield so that sufficient photons are detected to allow precise localization, and should be monomeric so that false multimers do not arise from self-aggregation. It should also undergo irreversible photoactivation so that each PA-FP is detected only once (24). Emission from an ideal PA-FP should also be continuous until photobleached. Unfortunately, this is rarely achieved with current-generation PA-FPs. Instead, emission from most PA-FP after initial photoactivation is interrupted by transient dark states (25). This complicates analysis because, during the dark periods of one PA-FP molecule, another PA-FP residing in close proximity may be activated and start to emit fluorescence. If two PA-FPs happen to be at a distance less than their localization accuracy and emit fluorescence in successive frames, it becomes difficult to distinguish between the two (26–29). This can be partially rectified by adjusting the photoactivation illumination intensity so that the time between photoactivation of two closely spaced PA-FPs is long compared with the lifetime of the dark states (T_{off}). In these circumstances, multiple emission events from the same molecule can be identified and combined by allowing the events to be separated by certain, transient durations of dark periods.

We selected PAmCherry1 as the PA-FP for this study because it has a relatively high photon yield, is monomeric, and undergoes irreversible photoactivation in bulk measurements (24). We tested the utility of PAmCherry1 as a reporter for quantitative PALM imaging by expressing it in BHK21 cells and imaging the cells after fixation. In this and subsequent applications, the activating beam was on continuously but at a low level. We observed that PAmCherry1 molecules enter transient dark states (i.e., blink). By using an approach suggested by Annibale et al. (26), we estimated that the average T_{off} (or time scale of blinking) of PAmCherry1 is ~0.26 ± 0.03 s (*SI Appendix*, Fig. S3). By comparison, the time separation between emissions from different PAmCherry1 molecules within the same resolution element is at least 20 s under the molecular densities in this investigation, assuming that activation of the molecules is completely stochastic. We dealt with blinking by combining multiple emission events from the same image location within 1.3 s (i.e., ~$5 \times T_{off}$) into one event: a short interval compared with the ~20-s interval between emissions expected from independent closely spaced PAmCherry1 proteins.

The resulting reconstructed PALM images of PAmCherry1 showed individual monomeric fluorophores randomly scattered throughout the cytoplasm, as expected. An example image is shown in Fig. 1*A*, where each dot represents the center of mass of one PAmCherry1 molecule. Visual inspection of this image indicated a predominant monomer distribution with few "clusters." A significant fraction of these clusters were artifacts attributable to particles randomly positioned in proximity, as demonstrated in Fig. S4*A*. For a more accurate estimation on the extent of clustering, we used the Ripley *K* test (30), which detects clustering by counting how many particles on average are found within a specified distance to a given particle and comparing that with predictions from a random spatial pattern. We determined that ~6% PAmCherry1 proteins would be scored as being in dimers or multimers (Fig. 1*B*). These apparent PAmCherry1 clusters may result from the presence of long-lived dark states that cause individual proteins to give rise to multiple events, or from slight multimer formation of PAmCherry1 molecules. In either case, the level of clustering is not so large as to preclude use of PALM imaging for assessment of biologically induced multimer formation.

We further explored the utility of PAmCherry1 as a quantitative PALM probe for assessment of multimer formation by imaging PAmCherry1–PAmCherry1, a genetically encoded artificial dimer. We expressed the dimer in BHK21 cells, imaged the cells after fixation, and processed and analyzed the data as described for PAmCherry1. The resulting images are very different from those of PAmCherry1. Specifically, PALM images of the artificial dimer showed a high number of PAmCherry1 pairs that we interpret to represent dimers (Fig. 1*C*). In accordance with visual inspection, a Ripley *K* test suggested that 77 ± 5% of PAmCherry1 molecules were in dimers, with the remaining ~23% in monomers (Fig. 1*D*). Note that, for this calculation, we assumed that PAmCherry1–PAmCherry1 forms only dimers because it is difficult to quantify the formation of higher-order multimers by using a Ripley *K* test.

We developed a spatial analysis method to assess the distribution of PAmCherry1 multimers from PALM images. The method combines computer simulations with the well-established density-based spatial clustering analysis with noise (DBSCAN) algorithm (31) and hence is named simulation-aided DBSCAN, or SAD. Briefly, DBSCAN classifies particles in the image into clusters based on particle density variations (Fig. 1*E*). We found that the assignments by DBSCAN were often inaccurate when there was significant positional noise in the data (*SI Appendix*, Figs. S4 and S5), which is typical in PALM images. SAD addresses this problem by using computer simulations to generate data sets that contain the same positional noise as the PALM image, analyzing both data sets with DBSCAN and comparing the results, adjusting the simulation parameters, and regenerating the simulated data set. This process iterates until DBSCAN results on both the simulated and the PALM data match. At that point, the cluster size distribution of simulated data are presumed to represent that of the actual data. As shown in *SI Appendix*, Figs. S4 and S5, SAD robustly returns the correct cluster size distributions on simulated data sets with known cluster size distributions and added positional noise.

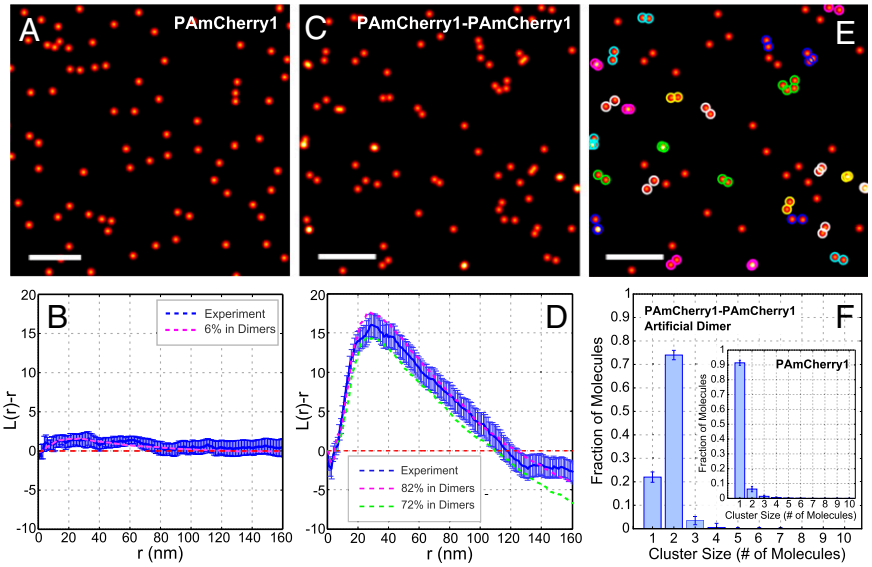

Fig. 1. Direct observation of protein dimers with PALM. (*A*) PALM image of PAmCherry1 expressed in a BHK21 cell. Each dot in the image represents one hypothetical PAmCherry1 molecule. (*B*) Ripley *K* test on PALM images of PAmCherry1. Test results from 21 images (~3 × 3 μm^2) at molecular densities of 80 ± 15 per square micrometer were pooled (thick blue line). The red dashed curve is Ripley *K* test on simulated data sets at the same molecular density, with ~6% of the molecules in dimers. (*C*) PALM image of PAmCherry1–PAmCherry1 artificial dimers expressed in a BHK21 cell. (*D*) Ripley *K* test on PALM images of PAmCherry1–PAmCherry1. Results from 17 (~2 × 2 μm^2) areas were pooled. (*E*) DBSCAN output of the image shown in *C*. Cluster diameter threshold is set at 37 nm. (*F*) Cluster size distributions in PALM images of PAmCherry1 and PAmCherry1–PAmCherry1 analyzed with SAD. (Scale bars: 200 nm.) All error bars represent SD.

We measured the cluster size distributions in PALM images of PAmCherry1 and the artificial dimer with SAD. For PAmCherry1, we found that 6 ± 3% of the molecules are in "dimers" and only a negligible fraction in larger clusters (Fig. 1*F*, *Inset*). For PAmCherry1–PAmCherry1, ~74% of PAmCherry1 are found in dimers and ~4% in trimers (Fig. 1*F*). In both cases, the fluorophore densities are approximately 100 per square micrometer. These results largely agree with our findings with the Ripley *K* test (Fig. 1 *B* and *D*). At higher fluorophore densities (148 ± 23 per square micrometer), SAD analysis of the dimer images yielded a similar cluster size distribution (*SI Appendix*, Fig. S6) to Fig. 1*F*.

We used these results to estimate the detection efficiency (i.e., the probe recovery rate, x) of PAmCherry1 in our PALM imaging experiments. In imaging the dimers, the probability of a dimer being detected as a dimer is x^2 if we assume that the two PAmCherry1 fluorophores in the same dimer are photoactivated independently. Similarly, the probability of a dimer being detected as a monomer is the probability of detecting one PAmCherry1 times the probability of not detecting the other, i.e., $x * (1 - x)$. Hence, the ratio between detected molecules in dimers vs. those in monomers is $x^2/[x * (1 - x)]$, or $x/(1 - x)$. As measured with SAD, the ratio is $x/(1 - x) \sim 74/26$, or $x \sim 0.74$. For an n-mer, the detection efficiency is $\sim(0.74)^n$. We corrected subsequent results with these factors.

These results demonstrated that PALM imaging coupled with quantitative spatial analysis provides sufficient resolution and detection efficiency to directly visualize protein dimers and multimers in intact cells expressing a suitable PA-FP probe such as PAmCherry1.

CRAF Protein Distribution Analysis. We used quantitative PALM imaging as described earlier to analyze the distribution of PAmCherry1–CRAF fusion proteins (*SI Appendix*, Fig. S2) in BHK21 cells transfected with the PAmCherry1–CRAF expression construct alone or along with $KRAS^{G12D}$. PAmCherry1 fusion proteins analyzed in the present study and their properties are presented in *SI Appendix*, Figs. S1 and S2 and Table S1. As CRAF interacts with active RAS on the cell membrane, we used the total internal reflection fluorescence (TIRF) illumination scheme for conventional fluorescence and PALM imaging so that only PAmCherry1–CRAF molecules on or within ~100 nm of the basal membrane were imaged.

Cells expressing only PAmCherry1–CRAF had the fibroblast-like morphology typical of BHK21 cells, and exhibited low signal intensity in TIRF images (Fig. 2*A*). PALM images of PAmCherry1–CRAF in these cells showed only approximately 20 molecules per square micrometer on the membrane (Fig. 2*B*) with minimal clustering (Fig. 2*E*). These findings are consistent with CRAF existing predominantly as a cytosolic monomer in $KRAS^{WT}$ cells (16). They also show that the PAmCherry1–CRAF fusion proteins have a low propensity to form multimers.

In contrast, cells coexpressing PAmCherry1–CRAF and $KRAS^{G12D}$ showed a substantial increase in PAmCherry1 signal in TIRF images (Fig. 2*C*), consistent with recruitment of RAF to the cell membrane by mutant RAS (32). Notably, most cells exhibit sharp membrane protrusions that resemble actin-rich filopodia or invadopodia (Fig. 2*C*, *Inset*) (33); these structures are only 100 to 200 nm wide, which is below the diffraction limit, making them difficult to study with conventional light microscopy. PALM images of these cells clearly demonstrated the existence of CRAF dimers and higher-order multimers (Fig. 2 *D* and *E*). A high frequency of dimers is apparent in Fig. 2*D*, as marked by DBSCAN in the upper half (above the dotted line) of the image. SAD analysis indicated that in addition to dimers, a significant fraction of PAmCherry1–CRAF resides in trimers and even higher-order multimers (Fig. 2*E*; Fig. 2*D*, arrows). These higher-order multimers have not been previously reported in studies using IP (12, 13, 15) or crystallography (11, 20), and their mechanistic importance is not clear. Overall, expression of $KRAS^{G12D}$ increased the density and the extent of clustering of membrane-associated CRAF molecules compared with the control (CRAF expression alone), so that the number of multimers (including dimers) per square micrometer area on the membrane increased from 0.5 to 13 (Fig. 2*E*). This switch-like increase in multimer CRAF formation is consistent with CRAF multimer formation being important in RAS-mediated activation of RAF/MAPK.

CatC Dimerization Dependent on an Intact Protein Interface. With the existence and involvement of CRAF dimers in RAS mediated activation confirmed, we next sought to identify the domain (s) that mediate RAF dimerization. Published studies indicated that CatC—CRAF with the N-terminal regions CR1 and CR2 truncated (*SI Appendix*, Fig. S2) but containing the catalytic domain—is a constitutively active kinase, caused likely by the elimination of N-terminal autoinhibition followed by spontaneous dimerization (12, 13, 34). Following this lead, we used PALM imaging to analyze CatC–CatC interactions in BHK21 cells transfected with PAmCherry1–CatC or PAmCherry1–Cat^{R401H} constructs (*SI Appendix*, Fig. S2 and Table S1) after fixation. The $CatC^{R401H}$ mutation was selected because it has been shown that the R401 residue mediates interactions between the two CatC protomers and that the R401H mutation disrupts CRAF dimerization (12, 13). We used PALM imaging with relaxed TIRF excitation to enable analysis of PAmCherry1–CatC

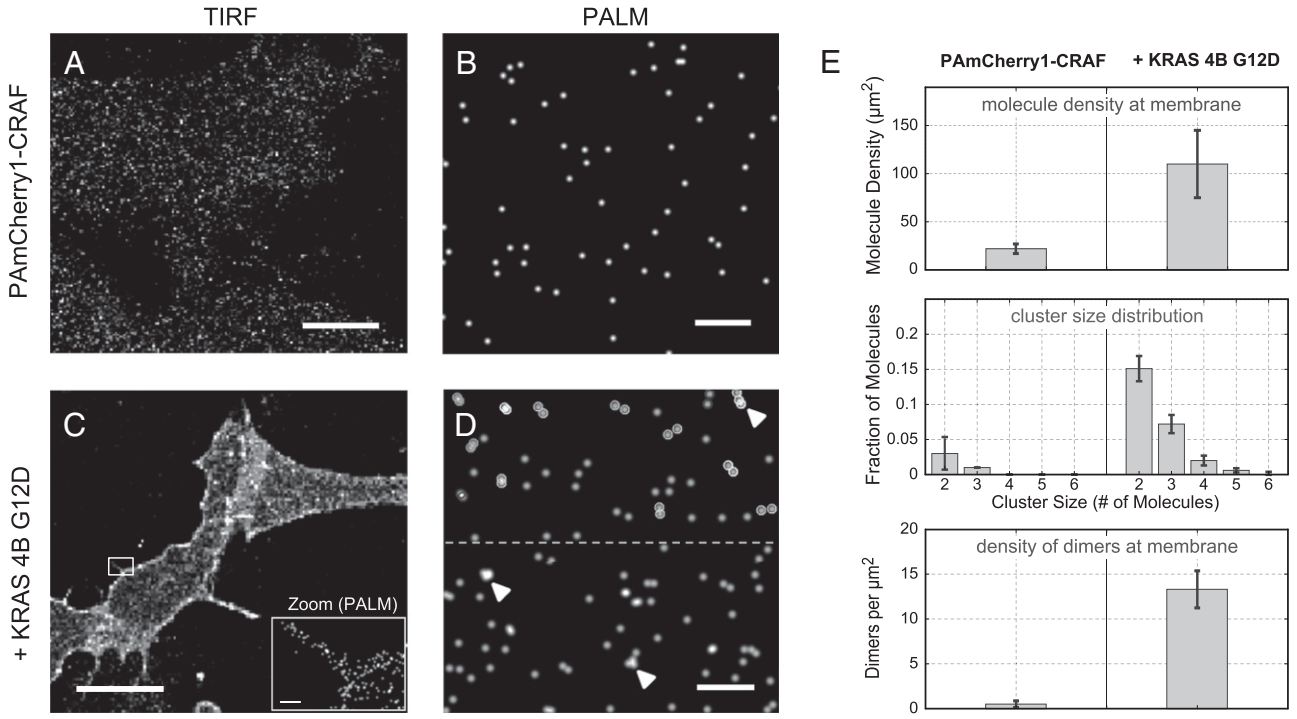

Fig. 2. Imaging CRAF dimers with quantitative PALM. (*A*) TIRF and (*B*) PALM images of PAmCherry1–CRAF expressed alone in BHK21 cells and (*C*) TIRF and (*D*) PALM images of PAmCherry1–CRAF coexpressed with $KRAS^{G12D}$. Individual clusters were marked based on DBSCAN results in the upper half of the image (above dotted line). Arrows indicate higher-order multimers. (*Inset*) Magnified PALM image of the area in the white box shows a membrane protrusion. (*E*) Comparisons between PAmCherry1–cRAF expressed alone (*Left*) and coexpressed with $KRAS^{G12D}$ (*Right*) on membrane localization (*Top*), cluster size distribution (*Middle*), and density of dimers (*Bottom*). (Scale bars: *A* and *C*, 5 μm; *C*, *Inset*, *B*, and *D*, 200 nm.)

proteins because CatC is predominantly cytosolic. Consistent with previous observations (11–13, 34, 35), PALM imaging showed that cytosolic PAmCherry1–CatC molecules did dimerize readily (Fig. 3*A*) whereas the PAmCherry1–$CatC^{R401H}$ mutant with disrupted CatC–CatC dimer interface dimerized to a much lesser extent (Fig. 3*B*). The difference remained at all expression levels examined, although multimerization of PAmCherry1–CatC and the R401H mutant increased at higher expression levels. The R401H mutant failed to active MAPK in BHK21 cells (*SI Appendix*, Fig. S8), highlighting the importance of dimerization in CatC activity.

SAD analysis further showed that PAmCherry1–CatC also forms tetramers. The cluster size distribution of cytosolic PAmCherry1–CatC (Fig. 3*C*), especially at the higher expression levels, is clearly different from that of full-length, membrane-bound RAF coexpressed with active RAS (Fig. 2 *D* and *E*). A major difference is that the frequency of trimers is much lower than tetramers in the case of PAmCherry1–CatC, suggesting that cytosolic CatC preferably forms tetramers rather than trimers. The PAmCherry1–CatC tetramers may be dimers of dimers mediated by an unidentified dimer interface additional to the one reported previously (11).

Our data strongly support the hypothesis that CatC spontaneously dimerizes without the need of membrane localization or active RAS, and suggest that the fundamental functional unit of CatC kinase is a dimer. As CatC is the kinase domain of CRAF, it is likely that the fundamental functional unit of full-length CRAF is also a dimer.

Multimerization of RAF-CAAX on the Cell Membrane. The difference in multimerization behavior between CatC and full-length CRAF (with $KRAS^{G12D}$) indicates that multimerization may proceed through different mechanisms in the two cases. We reason that the difference is likely a result of the N-terminal interactions of RAF or its interactions with RAS, as CatC is N-terminal truncated CRAF and does not bind RAS. The N-terminal of CRAF

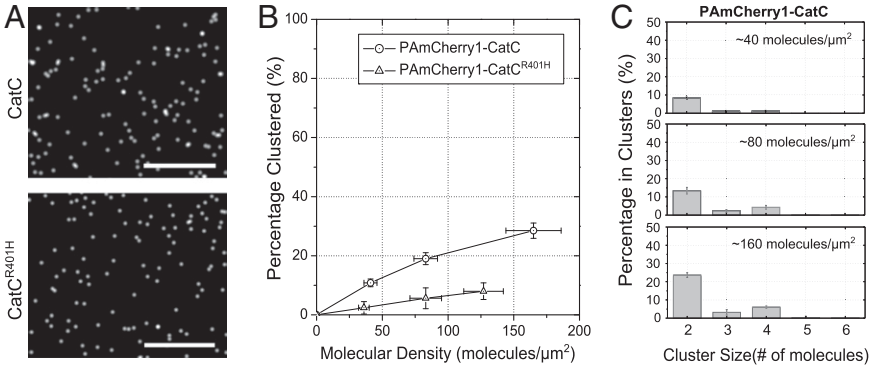

Fig. 3. CatC dimerization and its dependence on an intact dimer interface. (*A*) PALM image of PAmCherry1–CatC WT (*Upper*) and R401H mutant (*Lower*). (*B*) Comparison on clustered fractions of PAmCherry1–CatC WT (circles) and R401H mutant (triangles) measured at different molecular densities. (*C*) Cluster size distributions of CatC WT measured with SAD in PALM images at different molecular densities. (Scale bars: 500 nm.)

inhibits the kinase activation and dimerization (34, 36) so that RAS binding is a more plausible cause of observed RAF trimers in addition to dimers and tetramers in the presence of active RAS.

This view is supported by existing evidence. EM studies suggest that RAS itself clusters on the cell membrane, with a typical cluster size of four to eight RAS molecules, and that the clustering was mostly governed by its C-terminal ~20 residues known as the CAAX motif (37). When the RAS CAAX motif is attached to CRAF to create a chimeric protein CRAF–CAAX, the latter localizes to the cell membrane and becomes a constitutively active kinase (38, 39). These data suggest that CRAF–CAAX may be constitutively active because the CAAX motif drives CRAF into dimers and larger multimers. Similarly, CRAF molecules bound to active RAS could also dimerize or cluster through the RAS CAAX motif and display similar cluster sizes to RAS and different from that mediated by Cat–Cat domain interactions.

To better define the role of CAAX, we studied the clustering behavior of CRAF–CAAX by using quantitative PALM imaging. We fused the KRAS CAAX motif to PAmCherry1–CRAF and the R401H mutant to make PAmCherry1–CRAF–CAAX and PAmCherry1–CRAF^{R401H}–CAAX (*SI Appendix*, Fig. S2 and Table S1). The resulting chimeric proteins produced similar biological output to their untagged counterparts (Fig. 4*A*). Interestingly, PALM images of PAmCherry1–CRAF–CAAX (Fig. 4*B*, *Left*) and the R401H mutant (Fig. 4*B*, *Right*) obtained under stringent TIRF conditions clearly showed membrane-associated clustering. Cluster size distributions of the two proteins were similar, and are both akin to that of CRAF activated by KRAS^{G12D} but not to that of CatC, in that there is a higher population of trimers than tetramers. This implies that the CAAX motif indeed dominates the clustering of CRAF–CAAX and likely CRAF–KRAS^{G12D}.

These data also indicate that RAF multimer formation may not be sufficient for full MAPK activation because the RAS-derived CAAX motif did force formation of multimers of CRAF constructs carrying the dimer-interface R401H mutation but were less potent in stimulating ERK phosphorylation (an indicator of MAPK activity) than multimers formed by WT CRAF (Fig. 4*A*). A similar observation was previously reported on BRAF R509H dimer mutant, in which artificial dimerization of BRAF^{R509H} failed to activate MAPK as BRAF^{WT} did (11).

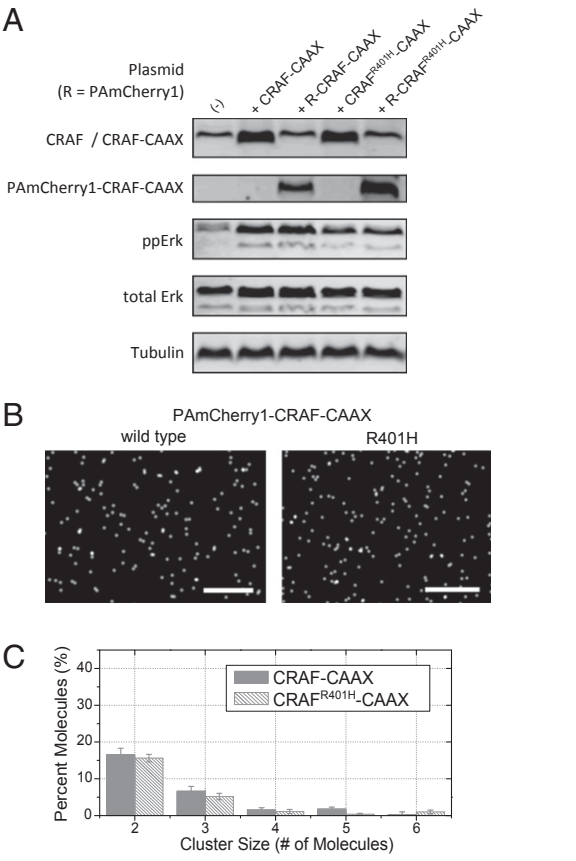

Fig. 4. Biological and clustering properties of PAmCherry1–CRAF–CAAX WT and R401H mutant. (*A*) BHK21 cells transfected with CRAF–CAAX (lane 2), PAmCherry1–CRAF–CAAX (lane 3), and the corresponding R401H mutants (lanes 4 and 5) were harvested and assayed for protein expression and MAPK pathway activation by Western blotting. Lysate from untransfected and serum-starved BHK21 cells was loaded as a control (lane 1). (*B*) PALM images of BHK21 cells transfected with PAmCherry1–CRAF–CAAX WT (*Left*) and R401H mutant (*Right*). (*C*) Comparison of cluster size distributions between PAmCherry1–CRAF–CAAX WT and R401H mutant measured with PALM/SAD. (Scale bars: 500 nm.)

Discussion

A full understanding of molecular mechanisms involved in the regulation of cell and tissue behavior requires information about molecular composition, molecular interaction, and multiscale molecular structures. Conventional biochemical, structural, and imaging tools have provided important insights into biological processes but do not provide direct information about key nanometer-scale regulatory architectures. We show here that nanometer-scale structures involved in RAS-mediated signaling can be studied in intact cells by using single-molecule superresolution imaging. Specifically, we demonstrated the utility of PALM in elucidating the role of CRAF multimer formation in RAS/MAPK signaling.

Studies of multimer formation require the ability to detect individual proteins with high efficiency. We explored the ability of PALM to resolve individual PAmCherry1-labeled CRAF proteins by imaging of PAmCherry1 and its artificial dimer (Fig. 1) in intact cells. With the assistance of new spatial analysis techniques including SAD, we estimated the detection efficiency of PAmCherry1 molecules to be ~74%. Although much lower than 100%, this is a significant improvement over other imaging techniques, especially those using antibodies in which the size of the probes typically limits the labeling efficiency to ~40% (37). The high fluorophore detection efficiency ensured successful imaging of dimers (at ~55% efficiency), trimers (~41%), and even tetramers (~30%). Our assessment of the utility of PALM imaging for single-molecule analysis in cells are consistent with other recent reports (26–29).

With the quantitative PALM imaging approach, we studied CRAF multimer formation under several MAPK activating conditions. RAF multimer formation has been suggested as an essential step in its activation in physiologic and pathologic signaling (11–13, 15). Previous studies have provided strong evidence for this hypothesis, but none have fully demonstrated the existence and spatial location of RAF dimers or their involvement in cellular processes. Our PALM imaging results showed unambiguously that CRAF forms multimers in all activating conditions tested, with dimers being the predominant multimer. In addition, we showed that RAF can form multimers by Cat–Cat (RAF catalytic domain) and by RAS–RAS interactions. In the latter case, it is the CAAX motif of RAS that drives clustering.

Another interesting finding of the present work is that multimer formation may not be sufficient to fully activate RAF. For example, CRAF^{R401H} fused to the RAS CAAX does form multimers on the membrane at approximately the same level as observed for CRAF–CAAX multimers. However, the extent of pErk up-regulation is lower for the R401H mutant compared with WT. Furthermore, although the biological activity of a RAF–RAF multimer depends on an intact interaction interface, some mutations of RAF such as V600E in BRAF appear to achieve an active conformation without multimer formation. Indeed, the BRAF$^{V600E,\ R509H}$ double mutant can still activate MAPK (14). In other words, RAF–RAF dimerization is only one of the possible routes to changing the protein conformation of RAF for its kinase activation.

In summary, we have used single-molecule superresolution imaging to directly visualize CRAF multimers under activating conditions and to assess the cellular locations in which these multimers form. Depending on the cellular or therapeutic context, RAF molecules may exhibit various multimer properties, including formation of dimers, trimers, and/or tetramers, of which the biological consequence is unknown. Our study demonstrates the power of quantitative single-molecule measurement in uncovering fine details of cellular processes at the molecular scale.

Materials and Methods

Plasmids. An entry clone (pENTR) of PAmCherry1 with both 5′and 3′ multicloning sites (MCSs) was generated by using a TOPO directional cloning kit (K2400-20; Life Technologies). A map of the entry clone is provided in *SI Appendix*, Fig. S1. PCR products of cDNAs of the genes of interest were then digested and inserted into one of the MCSs at the N or C terminus of PAmCherry1 in this entry clone. Expression clones were then generated by LR reaction (11791-020; Life Technologies) with a pcDNA3.1 destination vector.

Cell Culture and Transfection. BHK21 cells were obtained from American Type Culture Collection (catalog no. CCL-10), and maintained in high-glucose DMEM (no. 11965-092; Gibco) supplemented with 10% (vol/vol) FBS (no. 10437; Gibco) at 37 °C and 5% (vol/vol) CO_2. Cells were plated 24 to 48 h before transfection in six-well plates for Western blot or two-well chambered coverglass (no. 12-565-336; Thermo Fisher) with phenol red-free DMEM (no. 21063; Gibco) for imaging, at densities to reach ∼80% confluence on the day of transfection. The coverglass was pretreated with 1 M NaOH solution for 3 h and washed thoroughly with distilled water. For each well, a total of 1 μg plasmid DNA was transfected. Equal amounts of each plasmid were used for cotransfection experiments. For Western blot, cells were serum started overnight 24 h after transfection and harvested. Typically, 20 μg of total protein was loaded for each sample.

PALM Microscopy. PALM microscopy was performed on a custom setup. We used a 405-nm laser (CUBE-405; Coherent) for the photoactivation of PAmCherry1 and a 561-nm laser (MGL-H-561; OptoEngine, UT) for excitation. The typical power density used for photoactivation (405 nm) is 0.1 to 1.5 W/cm^2, and that for imaging (561 nm) is ∼1 kW/cm^2. The 405-nm laser remained on during image acquisition, with the power gradually increased to ensure complete photoactivation of all molecules within the field of view. We perform PALM imaging in 100 mM Tris buffer (pH 8.5) with 30 mM NaCl and 20 mM $MgCl_2$. Gold nanoparticles (100 nm) were added to the buffer before imaging as fiducial markers. Image and spatial analyses were performed with Matlab scripts.

ACKNOWLEDGMENTS. We thank Drs. Kevan Shokat [University of California, San Francisco (UCSF)], Chao Zhang (formerly of UCSF), Axel Brunger (Stanford University), Chao Zhang (Plexxikon), and Gideon Bollag (Plexxikon) for helpful discussions. Drs. Kevan Shokat and Chao Zhang also provided cDNAs for CRAF and CatC. This work was supported by National Institutes of Health (NIH) Grants K08 CA137153 (to E.A.C.) and 5U54CA143836 (to X.N. and T.M.T.; principal investigator, J.T.L.), National Science Foundation Grant PHY-0647161 (to X.N.; principal investigator, J.T.L., formerly S.C.), and a supplement grant to NIH U54 CA112970 (to X.N.; principal investigator, J.W.G.). Research in the laboratory of J.W.G. was supported by the Office of Science and the Office of Biological and Environmental Research, both of the US Department of Energy, under Contract DE-AC02-05CH11231, and by the W. M. Keck Foundation.

1. Wellbrock C, Karasarides M, Marais R (2004) The RAF proteins take centre stage. *Nat Rev Mol Cell Biol* 5(11):875–885.
2. Seger R, Krebs EG (1995) The MAPK signaling cascade. *FASEB J* 9(9):726–735.
3. Roberts PJ, Der CJ (2007) Targeting the Raf-MEK-ERK mitogen-activated protein kinase cascade for the treatment of cancer. *Oncogene* 26(22):3291–3310.
4. Schubbert S, Shannon K, Bollag G (2007) Hyperactive Ras in developmental disorders and cancer. *Nat Rev Cancer* 7(4):295–308.
5. McCormick F (2007) Success and failure on the ras pathway. *Cancer Biol Ther* 6(10): 1654–1659.
6. Su F, et al. (2012) RAS mutations in cutaneous squamous-cell carcinomas in patients treated with BRAF inhibitors. *N Engl J Med* 366(3):207–215.
7. Hansen JD, et al. (2008) Potent and selective pyrazole-based inhibitors of B-Raf kinase. *Bioorg Med Chem Lett* 18(16):4692–4695.
8. Tsai J, et al. (2008) Discovery of a selective inhibitor of oncogenic B-Raf kinase with potent antimelanoma activity. *Proc Natl Acad Sci USA* 105(8):3041–3046.
9. Nazarian R, et al. (2010) Melanomas acquire resistance to B-RAF(V600E) inhibition by RTK or N-RAS upregulation. *Nature* 468(7326):973–977.
10. Oberholzer PA, et al. (2012) RAS mutations are associated with the development of cutaneous squamous cell tumors in patients treated with RAF inhibitors. *J Clin Oncol* 30(3):316–321.
11. Rajakulendran T, Sahmi M, Lefrançois M, Sicheri F, Therrien M (2009) A dimerization-dependent mechanism drives RAF catalytic activation. *Nature* 461(7263):542–545.
12. Hatzivassiliou G, et al. (2010) RAF inhibitors prime wild-type RAF to activate the MAPK pathway and enhance growth. *Nature* 464(7287):431–435.
13. Poulikakos PI, Zhang C, Bollag G, Shokat KM, Rosen N (2010) RAF inhibitors transactivate RAF dimers and ERK signalling in cells with wild-type BRAF. *Nature* 464(7287):427–430.
14. Poulikakos PI, et al. (2011) RAF inhibitor resistance is mediated by dimerization of aberrantly spliced BRAF(V600E). *Nature* 480(7377):387–390.
15. Weber CK, Slupsky JR, Kalmes HA, Rapp UR (2001) Active Ras induces heterodimerization of cRaf and BRaf. *Cancer Res* 61(9):3595–3598.
16. Rushworth LK, Hindley AD, O'Neill E, Kolch W (2006) Regulation and role of Raf-1/B-Raf heterodimerization. *Mol Cell Biol* 26(6):2262–2272.
17. Farrar MA, Alberol-Ila J, Perlmutter RM (1996) Activation of the Raf-1 kinase cascade by coumermycin-induced dimerization. *Nature* 383(6596):178–181.
18. Luo Z, et al. (1996) Oligomerization activates c-Raf-1 through a Ras-dependent mechanism. *Nature* 383(6596):181–185.
19. Goetz CA, O'Neil JJ, Farrar MA (2003) Membrane localization, oligomerization, and phosphorylation are required for optimal raf activation. *J Biol Chem* 278(51): 51184–51189.
20. Bollag G, et al. (2010) Clinical efficacy of a RAF inhibitor needs broad target blockade in BRAF-mutant melanoma. *Nature* 467(7315):596–599.
21. Betzig E, et al. (2006) Imaging intracellular fluorescent proteins at nanometer resolution. *Science* 313(5793):1642–1645.
22. Hess ST, Girirajan TP, Mason MD (2006) Ultra-high resolution imaging by fluorescence photoactivation localization microscopy. *Biophys J* 91(11):4258–4272.
23. Rust MJ, Bates M, Zhuang X (2006) Sub-diffraction-limit imaging by stochastic optical reconstruction microscopy (STORM). *Nat Methods* 3(10):793–795.
24. Subach FV, et al. (2009) Photoactivatable mCherry for high-resolution two-color fluorescence microscopy. *Nat Methods* 6(2):153–159.
25. Ha T, Tinnefeld P (2012) Photophysics of fluorescent probes for single-molecule biophysics and super-resolution imaging. *Annu Rev Phys Chem* 63(1):595–617.
26. Annibale P, Vanni S, Scarselli M, Rothlisberger U, Radenovic A (2011) Quantitative photo activated localization microscopy: Unraveling the effects of photoblinking. *PLoS ONE* 6(7):e22678.
27. Greenfield D, et al. (2009) Self-organization of the Escherichia coli chemotaxis network imaged with super-resolution light microscopy. *PLoS Biol* 7(6):e1000137.
28. Sengupta P, et al. (2011) Probing protein heterogeneity in the plasma membrane using PALM and pair correlation analysis. *Nat Methods* 8(11):969–975.
29. Renz M, Daniels BR, Vámosi G, Arias IM, Lippincott-Schwartz J (2012) Plasticity of the asialoglycoprotein receptor deciphered by ensemble FRET imaging and single-molecule counting PALM imaging. *Proc Natl Acad Sci USA* 109(44):E2989–E2997.
30. Ripley BD (1977) Modelling spatial patterns. *J Royal Stat Soc B* 39(2):172–212.
31. Ester M, Kriegel H-P, Jörg S, Xu X (1996) A density-based algorithm for discovering clusters in large spatial databases with noise. *Proceedings of the 2nd International Conference on Knowledge Discovery and Data Mining* (AAAI Press, Menlo Park, CA), pp 226–231.
32. Marais R, Light Y, Paterson HF, Marshall CJ (1995) Ras recruits Raf-1 to the plasma membrane for activation by tyrosine phosphorylation. *EMBO J* 14(13):3136–3145.
33. Murphy DA, Courtneidge SA (2011) The 'ins' and 'outs' of podosomes and invadopodia: Characteristics, formation and function. *Natl Rev* 12(7):413–426.
34. Stanton VP, Jr., Cooper GM (1987) Activation of human raf transforming genes by deletion of normal amino-terminal coding sequences. *Mol Cell Biol* 7(3):1171–1179.
35. Heidecker G, et al. (1990) Mutational activation of c-raf-1 and definition of the minimal transforming sequence. *Mol Cell Biol* 10(6):2503–2512.
36. Cutler RE, Jr., Stephens RM, Saracino MR, Morrison DK (1998) Autoregulation of the Raf-1 serine/threonine kinase. *Proc Natl Acad Sci USA* 95(16):9214–9219.
37. Plowman SJ, Muncke C, Parton RG, Hancock JF (2005) H-ras, K-ras, and inner plasma membrane raft proteins operate in nanoclusters with differential dependence on the actin cytoskeleton. *Proc Natl Acad Sci USA* 102(43):15500–15505.
38. Leevers SJ, Paterson HF, Marshall CJ (1994) Requirement for Ras in Raf activation is overcome by targeting Raf to the plasma membrane. *Nature* 369(6479):411–414.
39. Stokoe D, Macdonald SG, Cadwallader K, Symons M, Hancock JF (1994) Activation of Raf as a result of recruitment to the plasma membrane. *Science* 264(5164):1463–1467.